A CFAR Detection Approach for Identifying Gas Bubble Seeps With Multibeam Echo Sounders

Thomas C. Weber, *Member, IEEE*

***Abstract*—A cell-averaged constant false alarm rate (CFAR) detector is described and applied to data collected with a multibeam echo sounder (MBES). The CFAR detector is designed specifically for transient targets observed with MBES, and operates under the assumption that background noise, including volume and seafloor reverberation, is locally stationary in time. This assumption, and the CFAR detector performance in general, was examined for data collected by a 30-kHz MBES operating in the Gulf of Mexico where the targets of interest were methane gas bubble plumes rising up from the seabed. Results with example data suggest that the CFAR detector was able to remove 99.1% of the MBES raw data while preserving the targets of interest. False detections appear randomly distributed throughout a single MBES ping, unlike the targets, and a within-ping target clustering algorithm was able to remove many of the false detections. In a single ping, an example is shown where the combined CFAR detector and a target cluster-size rule was able to reduce the number of false detections to 99.8% of the original data. The detector and cluster-size rules were applied to a sequence of approximately 400 pings, and two additional morphological rules based on the size and aspect ratio of the resulting target clusters were then applied to the detections to isolate the MBES backscatter intensity associated with gas bubbles. This combination of CFAR detector and simple morphological classification rules provides a useful way to detect gas bubble seeps or other transient targets.**

***Index Terms*—Constant false alarm rate (CFAR), gas bubble, multibeam echo sounder (MBES), seep.**

I. Introduction

MULTIBEAM echo sounders (MBESs) are active sonar systems that are commonly used for bathymetric surveying [1], for inferring properties of the seafloor based on the intensity of scattered "echoes" [2], and to make inferences about a variety of processes with manifestations in the ocean water column [3]. MBESs typically form tens to hundreds of individual adjoining beams, often organized in a contiguous "fan" that provides a wide field of view (e.g., angular extents that can exceed 100°), and an angular resolution that can be orders of magnitude smaller than the field of view. A common deployment strategy for MBES is to mount the system on a vessel hull, so that the center of the fan is oriented downward and the beams extend out in the across-track direction (i.e., perpendicular to the direction of vessel motion). This mounting strategy enables the use of these systems for mapping a "swath" of the ocean as the vessel moves along a track line. This strategy is the one used for the data shown in this article, although the methodologies described herein are expected to apply to other mounting orientations and configurations of beams [4].

An increasingly common application for MBES is the detection of methane gas bubbles in the ocean. Methane gas bubbles have been widely observed escaping from the seabed throughout the world's oceans from sources that are either biogenic, typically in shallow sediments, or thermogenic in deep sediments [5]. As they rise toward the surface, the gas bubbles undergo a complicated journey involving the transport of gas to/from aqueous solution [6], microbial oxidation within the ocean [7], [8], and, possibly, direct injection into the atmosphere. Acoustical echo sounders are often used for detecting, enumerating, and quantifying the amount and fate of methane gas moving from the seabed into and through the ocean water column [9]–[17], including the use of MBES [17]–[24]. These acoustical methods take advantage of the large impedance contrast between the gas in the bubble and the surrounding ocean water, and the associated high scattering strength, particularly at or above the bubble resonance frequency [25]. The data presented in the present work takes advantage of a particularly good match between MBES operating frequency and bubble resonance frequency, as described in [17].

Various methods have been proposed for detecting the presence of gas-bubble seeps in MBES data including classifying erroneous detections of seafloor depth as gas bubble seeps [18], visual scrutiny [17], [19], generating masks to remove areas of high reverberation and using a threshold based on sorted statistics (e.g., the median) [24], and for detecting other targets of interest (e.g., [26]). The purpose of the present work is to describe and analyze the application of a cell-averaged constant false alarm rate (CFAR) detector to MBES data, along with a simple morphology-based classification algorithm, for detecting seeps of free gas in MBES data. CFAR detectors have been used with MBES data before, including the use of an ordered statistic CFAR detection method operating on a single ping, as a function of angle [27], [28]. The present work extends this approach, and operates across time (pings) rather than space, as described in Section II.

CFAR detectors provide a means to generate a decision threshold, above which a signal of interest is assumed to be

Manuscript received March 27, 2020; revised October 10, 2020; accepted January 26, 2021. This work was supported by NOAA under Grant NA10NOS4000073 and Grant NA15NOS4000200.

Associate Editor: J. Cobb.

The author is with the Center for Coastal and Ocean Mapping, and with the Mechanical Engineering Department, University of New Hampshire, Durham, NH 03824 USA (e-mail: tom.weber@unh.edu).

This article has supplementary downloadable material available at https://doi.org/10.1109/JOE.2021.3056910, provided by the author.

Digital Object Identifier 10.1109/JOE.2021.3056910

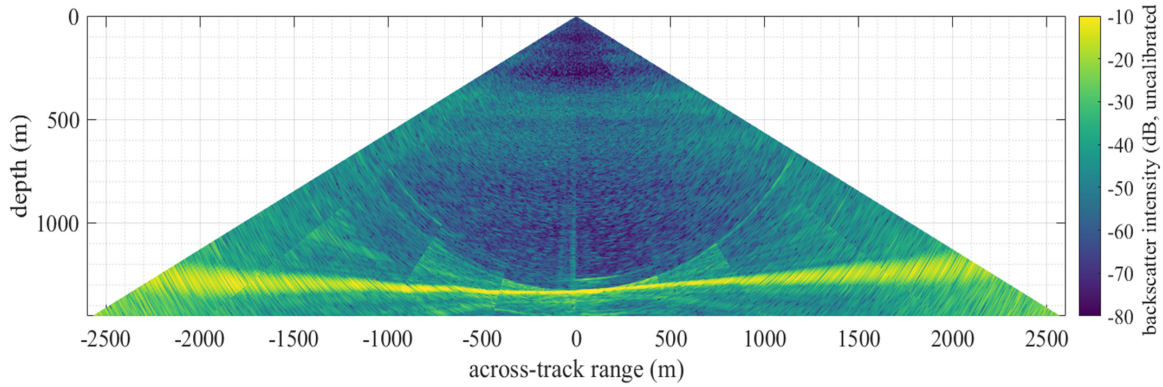

Fig. 1. Single ping from a 30-kHz MBES. Color represents the strength of the backscatter intensity from within the ocean volume and from the seabed (warmer colors represent higher backscatter). Seafloor backscatter is shown as the high-intensity "stripe" between 1200- and 1400-m depth.

present [29]. The main advantage of CFAR detectors, and that which is exploited in the present work, is that only knowledge of the noise (e.g., ambient noise, reverberation) is required to set the threshold, eliminating the need for *a priori* knowledge of the signal of interest. Several variations of CFAR detectors are available (e.g., [30]–[32]) with differences related to the manner in which the decision threshold is estimated. In general, the CFAR decision threshold is defined by some measure of the noise created by examining data in close proximity to the data for which a detection hypothesis test is being applied. For example, a statistic of the noise (e.g., mean, mean-square value, median) is estimated from a subset of data assumed to have no signal present. The decision threshold is then set at this statistic with some positive offset (e.g., twice the mean square value). Ideally, detections (observations with values above the decision threshold) are comprised only of the signal of interest, although in practical realizations of these methods the detections also include the upper portion of the distribution of the noise. Importantly, the portion of the noise distribution that will be above the decision threshold is predictable given some knowledge (sometimes assumed) of the underlying stochastic behavior of the noise, making it possible to determine the probability of false detections (i.e., false alarms). Further, under many conditions, the false detections are manifested randomly throughout a set of data (a "ping" in the present case), giving rise to "speckle noise" that can be further classified as being unlike a target for which multiple contiguous detections are likely.

This article is organized as follows. In Section II, a cell-averaged CFAR detector for MBES data is defined, applied to an example data set, and analyzed. This detector is particularly well-suited for transient (i.e., present in only one or a few pings) targets, but its use does not otherwise depend on specific target characteristics. This specificity is removed in Section III where a simple morphology-based classifier, operating on the detector output, is defined and used to identify detections that are associated with acoustical backscatter from gas bubble seeps. Finally, conclusions from this approach are drawn in Section IV.

II. Cell-Averaged CFAR Detector for MBES Data

Many MBESs utilize a Mills cross array topology, with orthogonal transmit and receive arrays, forming a fan of beams such as that shown in Fig. 1 [33], [34]. Scattered returns from targets within the water column can be observed when the target intensity is locally higher than the background noise and reverberation. The orthogonal transmit and receive arrays result in one-way sidelobe rejection, typically giving rise to high levels of seafloor reverberation at ranges equal to or greater than the shortest distance to the seafloor. Volume reverberation can also play a significant target-masking role in these data. When searching for gas bubble plumes, scattering from marine organisms often masks the return from the plumes. It is common, particularly in the deep ocean, for this volume reverberation to manifest as layers of increased scattering within isolated ranges of depth (i.e., the deep scattering layer [35]). Some MBESs, including the one used to generate Fig. 1, use multiple transmissions at similar but not identical frequencies across the angular region comprising a single ping. In the receiver beamformed data, these "sectors" appear as angle-dependent step-changes in receive sensitivity and background noise/reverberation. Taken together, noise in MBES appears spatially heterogeneous throughout the fan of beams, but is often locally stationary in time. That is, when considering data at a given location within the MBES fan, significant portions of both the volume and seafloor reverberation are statistically similar over several consecutive pings with the underlying assumption that the deep scattering layer and seafloor topology are slowly varying. This view of the MBES noise motivates the use of a cell-averaged detector where the average is conducted across several pings, and where the average is estimated independently for each range and angle.

A. Definition and Ideal Performance

To detect gas bubble plumes, or other transient targets, a cell-averaged CFAR detector was employed [29], [30]. The MBES raw data are stored as intensities in a 3-D matrix: sample number (range) $\times$ beam number (angle) $\times$ ping number. For a given ping, test cells are uniquely identified by their sample number and

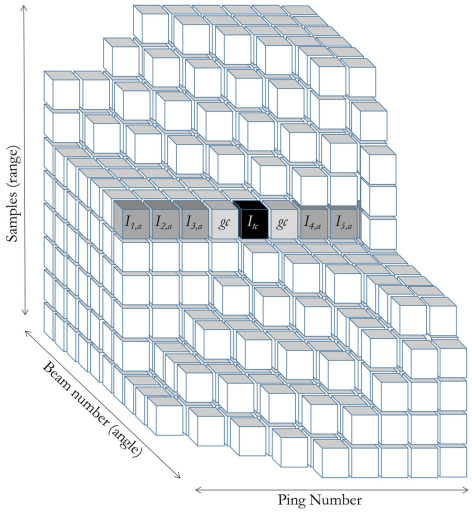

Fig. 2. Representation of the data collected from the MBES, with each cube representing a unique intensity value. The CFAR approach taken here compares the intensity in a test cell I_{tc} to the intensities in nearby pings $I_{i,a}$ with the exception of the immediate neighbors that are considered guard cells (gc).

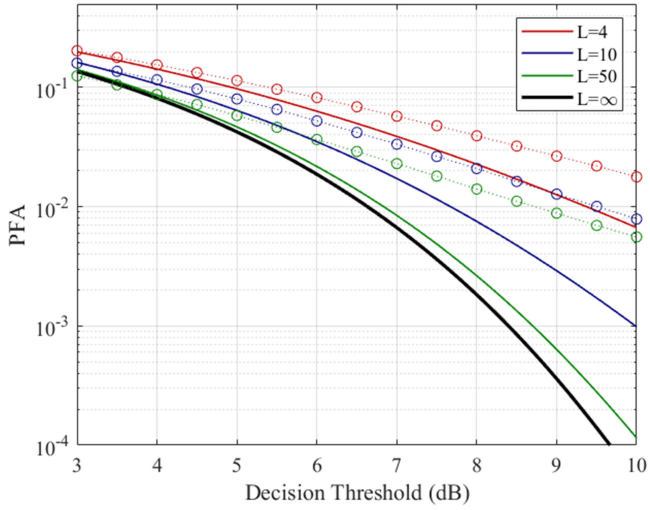

Fig. 3. Predicted probability of false alarms as a function of decision threshold, and for varying amounts L of auxiliary data (solid lines), after [30, Fig. 8.24]. Observations of the probability of false alarms for the data shown in Fig. 1, for the same numbers of auxiliary data, are overlaid as circles. Red line/circles: $L = 4$. Blue line/circles: $L = 10$. Green line/circles: $L = 50$. Black line: $L = \infty$.

beam number. Auxiliary data were selected from L other pings, evenly split between pings occurring before and after the test cell ping. The pings immediately adjacent to the test-cell ping were used as guard cells and were not included in the auxiliary data (see Fig. 2). Following [30, eq. (8.330)], the intensity in the test cell I_{tc} was then normalized by the average intensity in the auxiliary data $I_{i,a}$ to generate a test statistic x

$$x = \frac{I_{tc}}{\frac{1}{L}\sum_{i=1}^{L} I_{i,a}} \tag{1}$$

where the subscript a is an index referring to the unique sample number and beam number of x (i.e., the auxiliary data are chosen at the same sample number and beam number as the test cell).

Under the assumption that the received pressures in both the test cell and the auxiliary data are independent identically distributed Gaussian random variables in both their in-phase and quadrature components, I_{tc} can be scaled so that it follows a chi-squared distribution with 2 degrees of freedom and the denominator of (1) can be identically scaled to follow a chi-squared distribution with $2L$ degrees of freedom. The test statistic is then F-distributed with parameters 2 and $2L$. Knowledge of the distribution of x enables performance predictions for various choices of decision threshold (e.g., $x > 5$) and number of auxiliary data (i.e., size of L).

For a given decision threshold, the probability of a false detection (PFA) is simply the integral of the probability density function describing x at values greater than the threshold. The PFA is plotted for various numbers of auxiliary data, and for various thresholds, as shown in Fig. 3. Both an increased number of auxiliary data and increase in threshold reduce the PFA. One of the main advantages of this approach is that when the decision threshold is constant throughout the entire range-angle space, the false alarms are equally likely to appear throughout that entire space and manifest as "speckle," assuming that the statistical assumptions leading to the F-distribution were valid. One disadvantage is that it is not possible to analytically determine the probability of a missed detection: there is no target-based information in (1).

B. Example Performance: No Targets Present

To help assess the performance of the CFAR detector, the detector was applied to MBES data with no gas plumes present, selected based on manual scrutiny of the data. A single ping (see Fig. 1) was examined using threshold values corresponding to 3–10 dB, and for $L = 4$, 10, and 50. The MBES used to collect these data (Kongsberg EM 302) operates at a nominal frequency of 30 kHz and generates beams that are $1^\circ \times 1^\circ$ at broadside. MBES data were collected from the Mississippi Canyon in the Gulf of Mexico in 2011 [17]. Eight transmit sectors are used across the fan at frequencies ranging from 26 500 to 31 700 Hz. The boundaries of the transmit sectors, which are visible in Fig. 1, remain at constant receive beam angles throughout the data examined here. The MBES also transmits two sets of sectors, one steered slightly forward in pitch and one steered slightly aft, to increase the along-track coverage density. Each set operates at unique frequencies and only one set of sectors is considered here for simplicity. Operationally, the CFAR detector would operate uniquely on each set of transmit sectors and be subsequently combined. For example, the data would be separated into two unique subsets, one representing pitch-forward transmit sectors and one representing pitch-aft transmit sectors; the detector would be applied separately to each subset, and then the detector output for both subsets would recombined before any subsequent analysis steps. Because the detector input data sequence is across pings with beam number and sample range held constant (see Fig. 2), the fixed sector

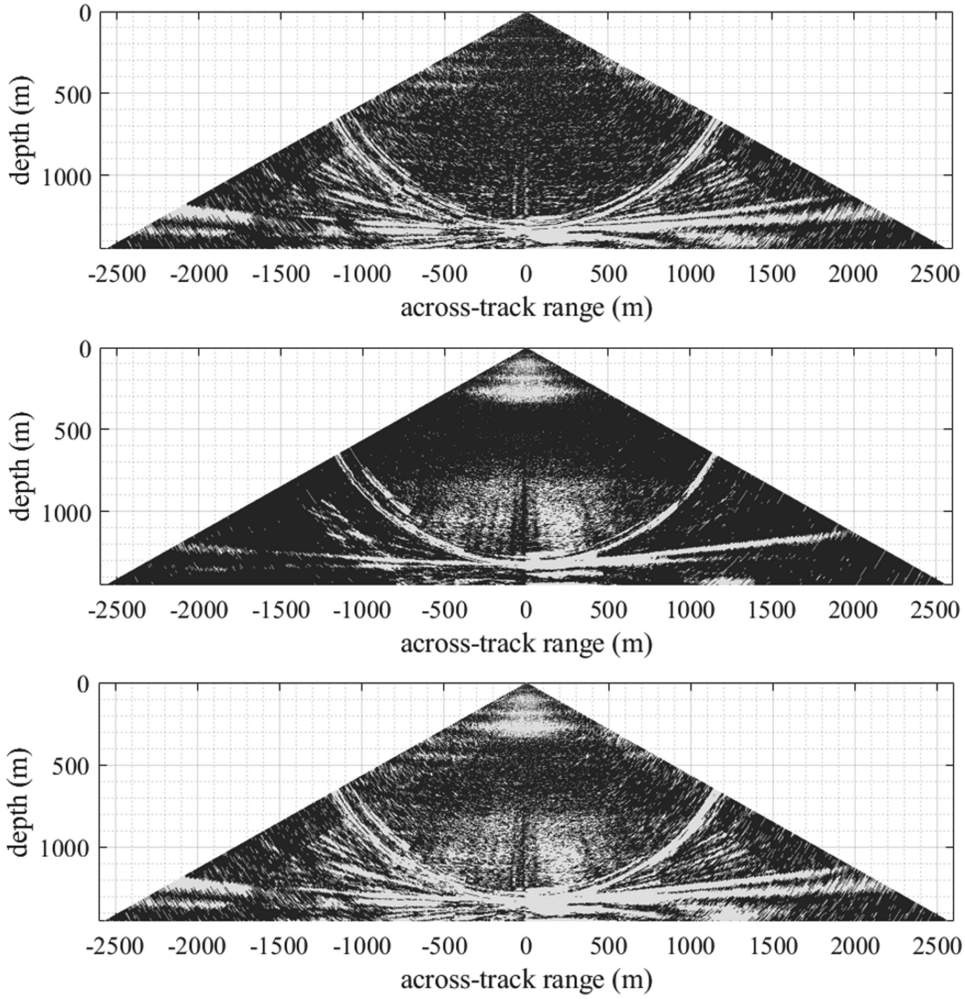

Fig. 4. Results of a reverse arrangement test for weak stationarity (top) and a Kolmogorov–Smirnov test for goodness of fit between the pressure amplitude data and a Rayleigh distribution (middle). In both cases, the test was run for 51 pings centered around the ping shown in Fig. 1, and light gray regions indicate that the test was rejected at the 5% significance level. The bottom image shows the regions (dark gray) where neither test was rejected.

boundaries present in the data examined here are expected to have no impact on the detector performance.

Before running the detector, two of the basic assumptions behind the performance model shown in Fig. 3 were tested: that the data were stationary, and that the underlying pressure amplitudes were Rayleigh distributed (or, equivalently, that the underlying intensity data can be scaled to follow a chi-squared distribution). Both assumptions were tested separately, as a function of sample and beam number, using +/–25 pings surrounding the single ping shown in Fig. 1, for a total of 51 pings. A reverse arrangement test [36] was used to test for weak stationarity, with the result shown in Fig. 4 (top). For the approximately 150 000 individual sample/beam locations shown in Fig. 4, 78% passed the reverse arrangement test at the 5% significance level. Within the region where volume reverberation dominates (i.e., at ranges less than 1300 m), the reverse arrangement test tended to fail at, or sometimes within, the boundaries of the horizontal scattering layers, with the regions of test failure often appearing much more limited in depth-extent than the layers themselves. This suggests that the layer boundaries were changing depth over the 51 ping sequence, and that the lack of stationarity in these regions may cause the CFAR detector to underperform. Test failure also occurred in the region of seafloor reverberation corresponding to the first return from the seabed (the constant range "ring" corresponding to the shortest range to the seabed) and to the seabed backscatter itself. This is likely due to the changing topography and/or seafloor substrate type in this area.

The pressure amplitudes corresponding to the same 51 pings used in the reverse arrangement test were compared to a Rayleigh distribution using a Kolmogorov–Smirnov goodness of fit test (KS-test). In each case (i.e., for each location in sample and range), the Rayleigh parameter was estimated from the mean. The KS-test failed to reject the hypothesis that the data were Rayleigh distributed for 77% of the individual sample/beam locations, including regions corresponding to both high volume and seafloor reverberation (Fig. 4, middle). The KS-test often failed in areas of seafloor reverberation where the reverse arrangement test also failed, as well as regions where the volume

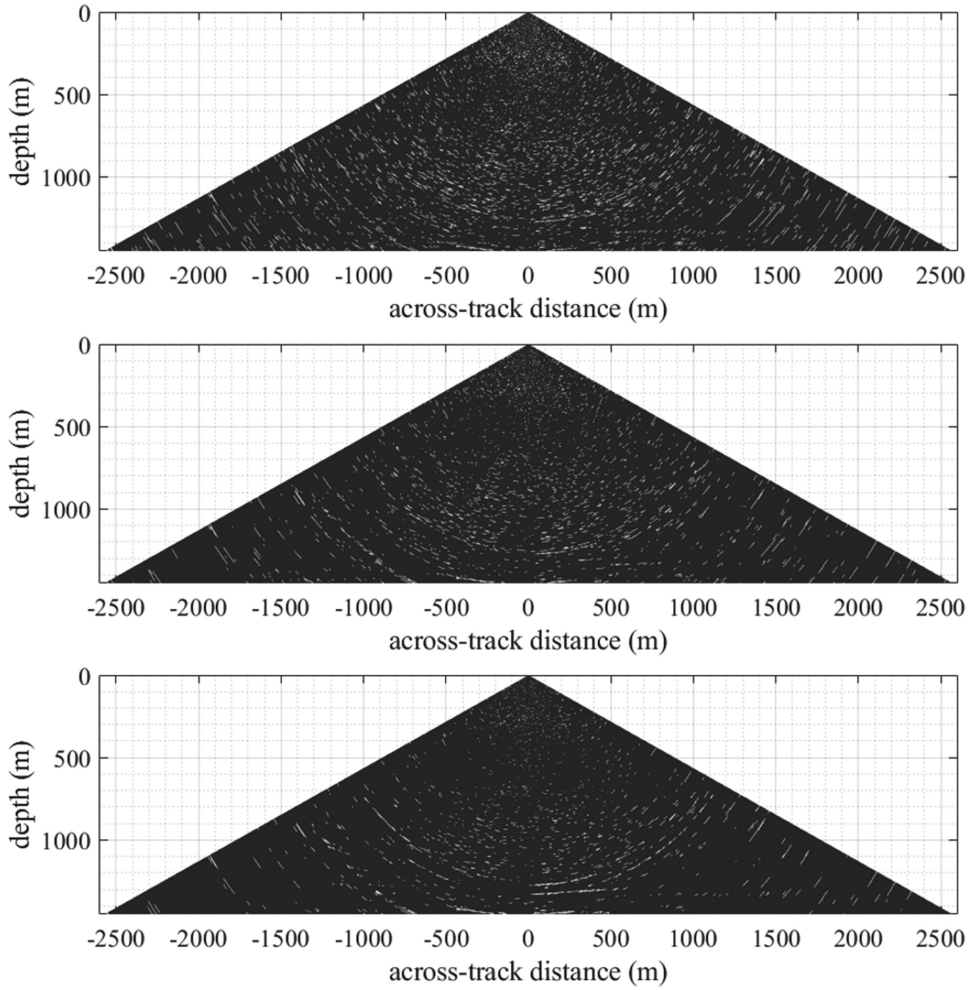

Fig. 5. Output of the detector for the ping shown in Fig. 1 where the decision threshold was set at $x = 5$, for different amounts of auxiliary data. Top: $L = 4$. Middle: $L = 10$. Bottom: $L = 50$. In each case, light gray indicates that the data exceeded the decision threshold and represents a false detection.

reverberation was very weak in-between and below scattering layers. The latter may be due to limitations of the recorded data, which "clip" below pressure amplitudes that would otherwise represent ambient or self-noise.

Neither the reverse arrangement test nor the KS-test was rejected for 62% of the data (Fig. 4, bottom), suggesting that the assumptions behind the CFAR detector performance may be valid over the majority of the MBES fan of beams. To examine this further, the detector was run on the data shown in Fig. 1 for a decision threshold of 7 dB (corresponding to $x \geq 5$) and for values of L corresponding to 4, 10, and 50, with the result shown in Fig. 5. Qualitatively, the noise passing through the detector appeared randomly distributed throughout the beam/angle space. Although there were some concentrated clusters of detections in areas that also exhibited strong seafloor reverberation, the contiguous regions where the reverse arrangement and KS-test failed were largely absent. However in each case, the observed probability of false detections exceeded that which would be predicted under the assumption that x was F-distributed with parameters 2 and $2L$. For $L = 4$, 10, and 50, the observed probability of false detections was 0.057, 0.033, and 0.023 rather than the predicted probabilities of 0.039, 0.017, and 0.0084, respectively, or between 1.5 and 3 times greater false detections. The detector was run for additional thresholds between 2 and 10 dB with the results shown in Fig. 3. In terms of the probability of false detections, the detector performance generally matched the predicted performance for low decision threshold, with an increasing difference between prediction and observation for higher decision thresholds. This trend generally suggests the data were heavier tailed than would be expected for Rayleigh distributed data, similar to that described in [37] and [38].

C. Performance: Targets Present

As a vessel traverses over the top of a gas bubble plume, the backscatter from the gas bubbles generally appears at a particular location within the fan of beams for only a few pings. Several such gas bubble plumes are shown in Fig. 6 (top) between +/–500 m in across-track range and below 500-m depth. The gas bubble plumes were narrow in across-track range and have

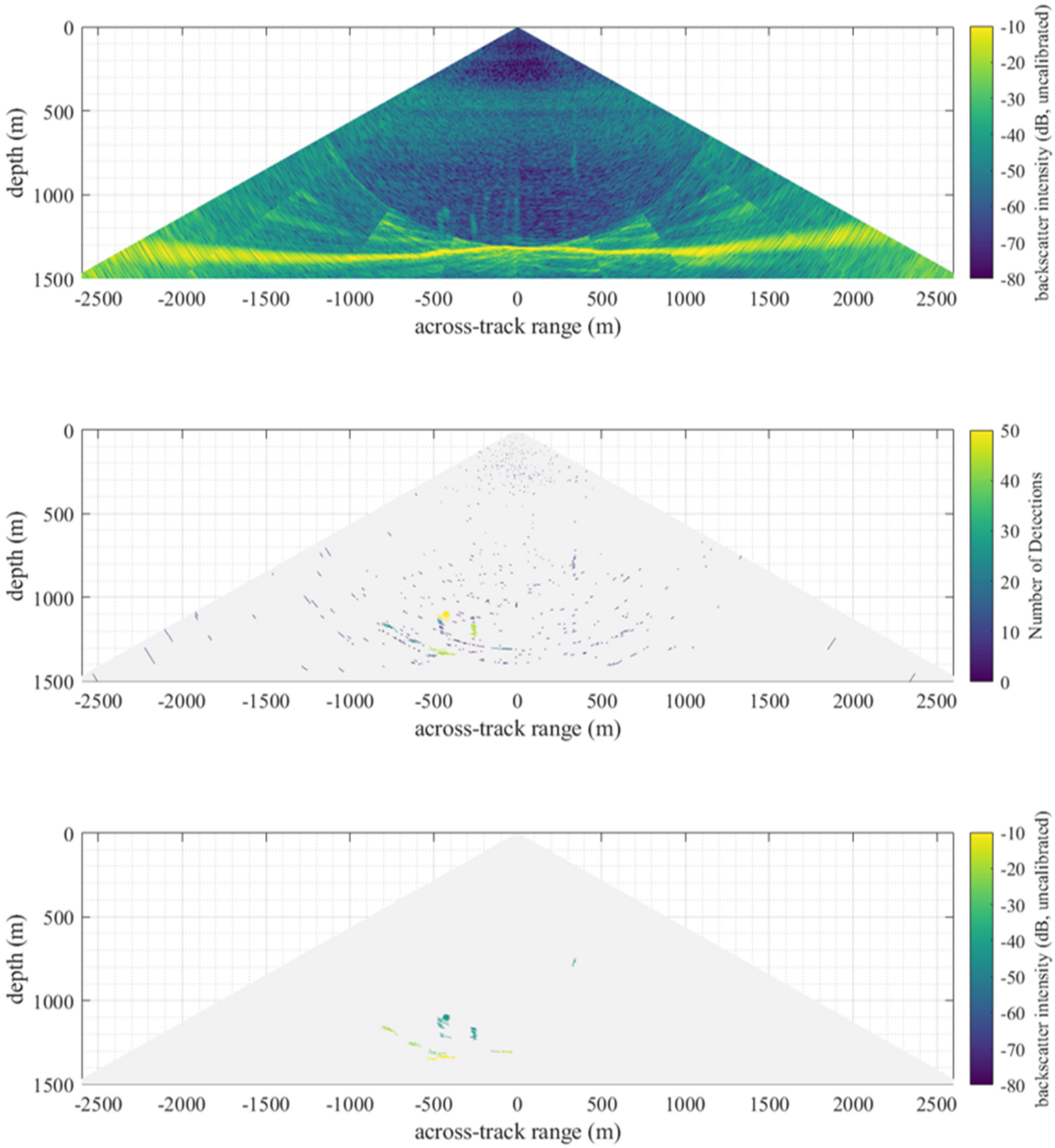

Fig. 6. (Top) Example MBES data exhibiting gas bubble plumes below 1000-m depth and between –200- and –500-m across-track range, and near 750-m depth and 500-m across-track range. Color corresponds to backscatter intensity in decibels. (Middle) The result of the CFAR detector with $L = 20$ and $x > 5$. The detector output is grouped into detection clusters. Color corresponds to the number of detections in a cluster. (Bottom) Only those detections where the number of detections in a cluster is 10 or more. Color corresponds to backscatter intensity in decibels.

a much greater vertical extent (100 m or more). Noise near the center beams at depths greater than 1000-m, similar to that shown in Fig. 1, was also present. The backscatter intensity from the bubbles was similar to, and sometimes weaker than, much of the volume and seafloor reverberation present throughout the data. A fixed intensity threshold set a level chosen to detect if the gas bubbles would provide a large percentage of false detections. However, experience has shown that it is relatively easy to manually identify gas bubble plumes in data such as these, and this is likely because the gas bubble targets are transient and unlike the surrounding noise, that is, they lend themselves well to the type of normalization underlying a CFAR detection approach.

The data shown in Fig. 6 (top) were run through a cell-averaged CFAR detector (see pseudocode in supplementary material). The detector used 20 auxiliary data ($L = 20$), evenly split between previous and following pings, two guard cells before the ping and two guard cells following the ping, and a decision threshold of $x > 5$. The number of guard cells is specific to the data being examined here, where backscatter from a gas

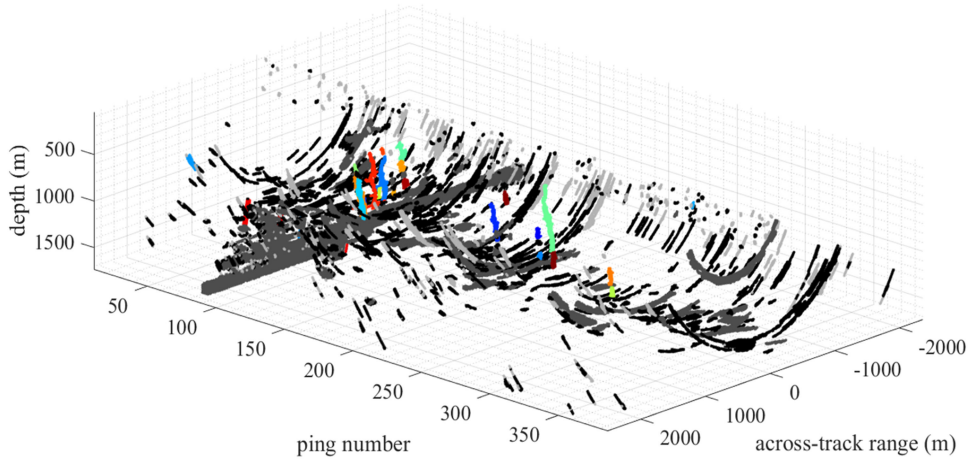

Fig. 7. Result of the CFAR detector and the minimum cluster-size rule on approximately 400 sequential pings of MBES data. Clusters classified as gas-bubble plumes are shown in color; clusters that had range extents less than 50 m and aspect ratios less than one are shown in black; clusters that had aspect ratios greater than one but range extents less than 50 m are shown in light gray; and clusters that had range extents greater than 50 m but aspect ratios less than one are shown in dark gray.

bubble plume is often observed at the same location within the fan of beams for two and occasionally three sequential pings. The resulting detections, shown in Fig. 6 (middle), show that the region corresponding to the gas bubbles has remained largely intact (i.e., has passed through the detector), and that the areas corresponding to the seafloor and volume reverberation were largely absent with the exception of random "speckle" data that were spread throughout the image. Of the original data, 0.9% (1353 out of the 153 486 unique sample numbers and beams shown in Fig. 6) were considered detections.

Visual scrutiny of the data, ping by ping, makes it possible to determine which of the detections corresponds to the rising gas bubbles. This is in part due to the tendency for false detections to appear as small groups, or clusters, of data, and for the rising gas bubbles to appear as larger contiguous regions of detections. The color scale in Fig. 6 (middle) corresponds to the detection cluster sizes, where a detection cluster is defined as a group of detections within a single ping that are contiguous in sample and beam space. In this case, the rules for generating a within-ping cluster (see pseudocode in supplementary material) were that there could be no gaps between beams, and at most a one-sample gap (3.5 m) in range. Out of the 506 clusters shown in Fig. 6 (middle), only 12 contained 10 or more detections. These 12 are shown in Fig. 6 (bottom), and include both regions corresponding to the gas-bubble plumes as well as seafloor reverberation. The combination of both CFAR detector and within-ping cluster-size threshold appear to preserve regions corresponding to gas-bubble seeps while reducing the detection opportunities (i.e., number of unique samples remaining) to 0.2% of the original data.

In this example, the combined detector and within-ping cluster-size threshold worked best for the gas bubble plumes visible at an across-track range between –200 and –500 m and below 1000 m. By contrast, only a portion of the gas bubble plume located at 400-m across-track range and 750-m depth passed through the process to be visible in Fig. 6 (bottom). This shallower seep exhibited generally 5 dB lower backscatter intensity and presented more generally as separated targets with smaller cluster sizes. This gas bubble plume remains manually observable throughout its vertical extent because of the vertical ordering of the targets, and it is possible that a more sophisticated classifier could use this ordering to link the targets together. However, it is worth noting that the lower portions of this particular gas bubble plume were detected in the subsequent eight pings and appear in Fig. 8 as the orange-colored plume (the green top of the plume corresponds to the ping associated with Fig. 6).

III. Simple Morphology-Based Classifier

Despite the large reduction in data from the combined CFAR detector and within-ping cluster-size threshold, the results for multiple sequential pings combine to create a large number of false detections. An example of the reduction for approximately 400 sequential pings is shown in Fig. 7, where ping number 30 is shown in Fig. 1 and ping number 99 is shown in Fig. 6. Plotted together, the false detections can obscure those associated with gas-bubble plumes. Many detections appear at constant ranges (i.e., constant radius of curvature) and are presumably associated with sidelobes and seafloor reverberation. Smaller (relative to the seafloor reverberation) groups of detections, presumably marine organisms, are present in the upper portion of the water column. Groups of detections that are narrow in horizontal extent and extend hundreds of meters vertically are also present, and these detections are the targets of interest (i.e., gas-bubble plumes).

To add a simple morphology-based classifier to the detections, the data shown in Fig. 7 were first clustered in three dimensions. All contiguous detections with no gaps of more than 20 m horizontally in the across-track direction, 30 m in the along-track direction (e.g., in the direction of the vessel) or 10 m in depth were uniquely labeled as individual clusters. For these data, the beams were spaced uniformly across the fan with a spacing of

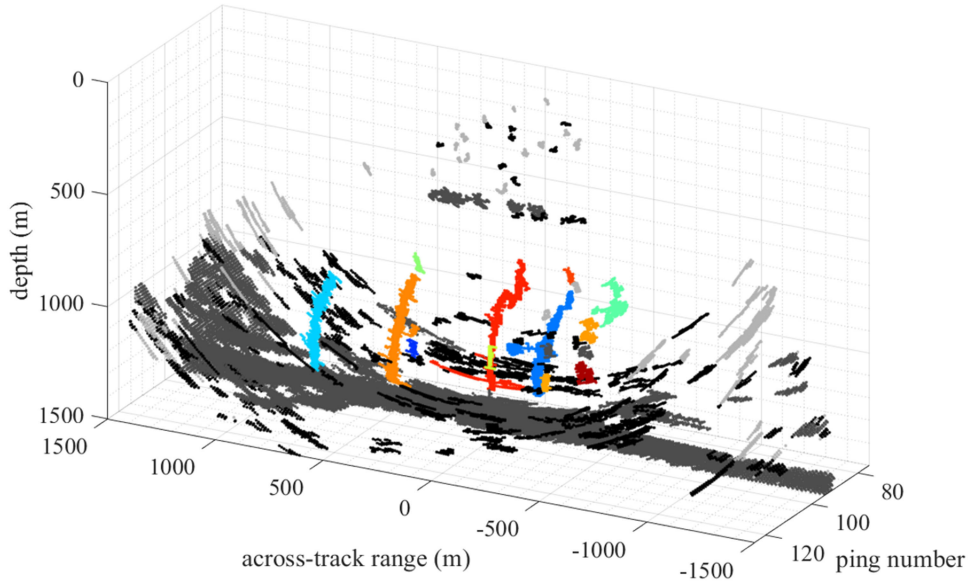

Fig. 8. A 20-ping subset of the results shown in Fig. 7. Clusters classified as gas-bubble plumes are shown in color; clusters that had range extents less than 50 m and aspect ratios less than one are shown in black; clusters that had aspect ratios greater than one but range extents less than 50 m are shown in light gray; and clusters that had range extents greater than 50 m but aspect ratios less than one are shown in dark gray. Ping 99 is also shown in Fig. 6.

0.4° between adjacent beams, and the 20 m horizontal gap corresponds approximately to double the spacing of beams near the seabed. Note that in the broadside direction, the beam resolution of the MBES is 1° in the across track direction, doubling to 2° in the outer portion of the fan, suggesting that backscatter intensities associated with single targets are likely to appear in at least two adjacent beams. During the collection of these data, the vessel traveled with near-constant speed of 4.6 m/s. The pings time ranged between 4.3 and 4.9 s, which effectively means that the 30-m along-track gap translated to a rule by which any groups of detections separated by at least one ping receive different 3-D cluster labels. In the range direction, the sample rate of the recorded MBES data corresponds to a resolution of 3.5 m (i.e., there is one sample every 3.5 m along each beam). A 10-m gap in depth allows for two or more detections containing a 2–3 sample region with no detections to be considered part of the same 3-D cluster. Considering a nominal bubble rise speed of 20 cm/s [39], a gas bubble released from the seabed at a rate faster than one bubble every 50 s would have vertical gaps less than 10 m, and detections associated with a gas plume with a slower release rate would not be grouped into the same 3-D cluster.

Only those 3-D clusters containing at least 25 detections were considered as possible gas-bubble plumes. This minimum number of detections is chosen to remove small detection 3-D clusters assumed to represent biological or other targets that were not of interest. In the present case, "small" corresponds to a vertical extent of less than 50 m (∼3% of the water depth) assuming that targets are detected in two adjacent beams. The *a priori* assumption is that the gas bubble plumes present at the study site had greater vertical extents.

Two morphological characteristics were calculated for each cluster: the range extent (maximum range minus minimum range, where range is measured along the beam) and the aspect ratio (maximum depth extent divided by the maximum across-track extent). Clusters associated with gas-bubble plumes were assumed to be only those that had a minimum range extent of 50 m and a minimum aspect ratio of 1. The objective of the range extent limit was to identify and remove clusters that appeared related to sidelobes (seafloor reverberation) at constant range, and to remove smaller clusters such as those that might be associated with the deep scattering layer, with the underlying assumption that gas bubble plumes would appear distributed in range. The objective of the aspect ratio limit was to remove clusters that had large range extents but that did not exhibit the expected tall, narrow cluster morphology associated with a gas bubble plume, such as that associated with the seabed return. Underlying the aspect ratio limit is the assumption that the horizontal currents in the deep ocean are no greater than the rise speed of the bubbles within the plumes.

The results of the morphology-based classifier are shown in Fig. 7, demarcated by color. A closer view of the region containing multiple gas bubble plumes near ping 100 is shown in Fig. 8. The results shown from the approximately 400 sequential pings are the outcome of the following four stages of processing (see pseudocode in supplementary material):

1) the CFAR detector with $L = 20$ and $x > 5$;
2) a within-ping minimum cluster size of ten detections, similar to that shown in Fig. 6 (bottom);
3) a minimum 3-D cluster size of 25 detections to group targets appearing across multiple pings;
4) the minimum range extent and aspect ratio limits of 50 m and 1, respectively.

The results suggest that this set of processing criteria has worked well to isolate targets associated with the gas bubble plumes. The small clusters of targets in the upper water column

(<500-m depth) were all excluded from further consideration due to a small range extent (light gray) or a combination of small range extent and low aspect ratio (black), except for one cluster near ping number 330 that passed all criteria, and several larger clusters near ping 90 that were excluded based on aspect ratio. Almost all of the seafloor reverberation was excluded, except for a target cluster near ping 10 at 1000-m water depth. Several other target clusters of unknown origin, located at ping numbers less than 100 and across-track ranges near 400 m, also appear to be falsely classified as gas bubble plumes.

All gas-bubble plumes present in the data, as assessed by an experienced observer, appear to have been detected. The four processing stages described above correctly identified groups of gas bubble plumes near ping 100, near ping 200, and near ping 275. It is possible to identify regions that have backscatter intensities that can be manually identified as being caused by the gas bubbles, but in these cases the same plume was detected on preceding or subsequent pings (see animated gif in supplemental data). Some individual gas bubble plumes are detected with multiple 3-D clusters, and so it may be advantageous to run a second clustering algorithm with a larger gap size to join these clusters. By contrast, in one case (Fig. 8, red-colored plume) the backscatter intensities associated with the rising bubble plumes were grouped with apparent seafloor reverberation, a scenario that would require some form of further processing to rectify in an automated scenario. Additional false alarms occur near the rising bubble plumes, where noise that has passed through the detector is within the along-track, across-track, and depth gap limits. These false alarms may cause small errors in the apparent width or height of the plume but, for the data examined here, have not caused the false rejection of a gas bubble plume due to errors in plume morphology. A 3-D cluster may also appear erroneously wide due to erroneous detections from sidelobes on beams adjacent to the actual plume.

IV. Conclusion

MBESs are increasingly used for detecting targets within the water column, and consequently different techniques for detecting and classifying targets are being established. Here, a cell-averaged CFAR detector using guard cells was described and analyzed. The detector used here uses auxiliary data collected from pings occurring both before and after the ping being examined, and consequently relies on the background noise being locally stationary in time. Furthermore, this detector is designed for transient targets that are unlike the background noise. That is, targets that are present in some sample/beam location throughout the auxiliary data would be erroneously considered background noise and would not pass through the detector. For the same reason, guard cells become an important aspect of the CFAR detector, reducing the likelihood that targets may be present in adjacent pings, a condition that might be expected to commonly occur for MBES that have low along-track resolution, for slow vessel transit speeds, and/or for combinations of the two. The methane gas bubble seeps examined here were considered transient targets in that they appeared at specific sample/beam location for only a few pings. This detection technique would not be suited for diffuse targets (e.g., diffuse gas bubble seeps, the deep scattering layer) unless auxiliary data were chosen by some other means, perhaps in a location that did not contain the targets of interest.

The CFAR detector by itself is useful for reducing the amount of data down to a few percent (or less) that are classified as detections, but even this reduction leaves many targets that must be classified. One helpful feature of the CFAR detector is that the false detections often appeared randomly distributed in space, unlike the targets of interest that appeared in larger clusters within an individual ping. In this work, the combination of the CFAR detector and a minimum within-ping cluster size was useful in reducing the number of false detections down to a fraction of a percent of the raw data. When pings were combined into a 3-D data set, two simple morphological parameters were able to eliminate almost all false detections while preserving the targets of interest. The morphological parameters used here were based on the minimal assumption that the gas bubble plumes would be tall and narrow, and would have a range extent that was at least 50 m (a few percent of the depth), target properties that worked well for this data set but that may need to be modified for other scenarios (e.g., different water depths, different echo sounders, different targets). In general, this combination of CFAR detector and simple morphological classification rules provides a useful way to detect gas bubble seeps or other transient targets.

Acknowledgment

The author would like to thank B. Calder for helpful comments on a draft of this manuscript. Data were collected aboard the NOAA *Okeanos Explorer* and are available at the NOAA National Center for Environmental Information repository, doi: 10.7289/V5736NW3, line 0533 collected on September 9, 2011.

References

[1] L. Mayer, "Frontiers in seafloor mapping and visualization," *Mar. Geophys. Res.*, vol. 27, no. 1, pp. 7–17, 2006.

[2] X. Lurton and G. Lamarche, Eds., "Backscatter measurements by seafloor-mapping sonars," Guidelines and Recommendations, 200p, May 2015. [Online]. Available: http://geohab.og/wp-content/uploads/2014/05/BSWGREPRT-MAY2015.pdf

[3] K. Colbo, T. Ross, C. Brown, and T. Weber, "A review of oceanographic applications of water column data from multibeam echosounders," *Estuarine, Coastal Shelf Sci.*, vol. 145, pp. 41–56, 2014.

[4] R. J. Korneliussen, Y. Heggelund, I. K. Eliassen, O. K. Øye, T. Knutsen, and J. Dalen, "Combining multibeam-sonar and multifrequency-echosounder data: Examples of the analysis and imaging of large euphausiid schools," *ICES J. Mar. Sci.*, vol. 66, no. 6, pp. 991–997, 2009.

[5] A. G. Judd, "Natural seabed gas seeps as sources of atmospheric methane," *Environ. Geol.*, vol. 46, no. 8, pp. 988–996, 2004.

[6] D. F. McGinnis, J. Greinert, Y. Artemov, S. E. Beaubien, and A. Wüest, "Fate of rising methane bubbles in stratified waters: How much methane reaches the atmosphere?" *J. Geophys. Res., Oceans*, vol. 111, no. C9, pp. 1–15, 2006.

[7] S. Mau, D. Valentine, J. Clark, J. Reed, R. Camilli, and L. Washburn, "Dissolved methane distributions and air-sea flux in the plume of a massive seep field, Coal Oil Point, California," *Geophys. Res. Lett.*, vol. 34, no. 22, pp. 1–5, 2007.

[8] W. S. Reeburgh, "Oceanic methane biogeochemistry," *Chem. Rev.*, vol. 107, no. 2, pp. 486–513, 2007.

[9] R. Merewether, M. S. Olsson, and P. Lonsdale, "Acoustically detected hydrocarbon plumes rising from 2-km depths in the Guayamas Basin, Gulf of California," *J. Geophys. Res.*, vol. 90, pp. 3075–3085, 1985.

[10] L. Dimitrov and V. Dontcheva, "Seabed pockmarks in the southern Bulgarian Black Sea Zone," *Bull. Geol. Soc. Denmark*, vol. 41, pp. 24–33, 1994.
[11] J. Hornafius, D. Quigley, and B. Luyendyk, "The world's most spectacular marine hydrocarbon seeps (Coal Oil Point, Santa Barbar Channel, California): Quantification of emission," *J. Geophys. Res.*, vol. 104, pp. 20703–20711, 1999.
[12] I. MacDonald, I. L. R. Sassen, P. Stine, R. Mitchell, and N. J. Guinasso, "Transfer of hydrocarbons from natural seeps to the water column and atmosphere," *Geofluids*, vol. 2, pp. 95–107, 2002.
[13] K. Heeschen, A. Trehu, R. Collier, E. Suess, and G. Rehder, "Distribution and height of methane bubble plumes on the Cascadia Margin characterized by acoustic imaging," *Geophys. Res. Lett.*, vol. 30, pp. 1–4, 2003.
[14] J. Greinert, Y. Artemov, V. Egorov, M. De Batist, and D. McGinnis, "1300-m-high rising bubbles from mud volcanoes at 2080 m in the Black Sea: Hydroacoustic characteristics and temporal variability," *Earth Planet. Sci. Lett.*, vol. 244, pp. 1–15, 2006.
[15] M. Römer, H. Sahling, T. Pape, G. Bohrmann, and V. Spieß, "Quantification of gas bubble emissions from submarine hydrocarbon seeps at the Makran continental margin (offshore Pakistan)," *J. Geophys. Res., Oceans*, vol. 117, no. C10, pp. 1–19, 2012.
[16] P. Kannberg, A. Tréhu, S. Pierce, C. Paull, and D. Caress, "Temporal variation of methane flares in the ocean above Hydrate Ridge, Oregon," *Earth Planet. Sci. Lett.*, vol. 368, pp. 33–42, 2013.
[17] T. Weber, L. Mayer, K. Jerram, J. Beaudoin, Y. Rzhanov, and D. Lovalvo, "Acoustic estimates of methane gas flux from the seabed in a 6000 km^2 region in the northern Gulf of Mexico," *Geochem., Geophys., Geosyst.*, vol. 15, no. 5, pp. 1911–1925, 2014.
[18] J. Schneider von Deimling, J. Brockhoff, and J. Greinert, "Flare imaging with multibeam systems: Data processing for bubble detection at seeps," *Geochem., Geophys., Geosyst.*, vol. 8, no. 6, pp. 1–7, 2007.
[19] A. Nikolovska, H. Sahling, and G. Bohrmann, "Hydroacoustic methodology for detection, localization, and quantification of gas bubbles rising from the seafloor at gas seeps from the eastern Black Sea," *Geochem., Geophys., Geosyst.*, vol. 9, no. 10, pp. 1–13, 2008.
[20] J. Gardner, M. Mashkoor, and S. Walker, "Plume 1400 meters high discovered at the seafloor off the northern California margin," *Eos, Trans. Amer. Geophys. Union*, vol. 90, no. 32, p. 275, 2009.
[21] J. Schneider von Deimling and C. Papenberg, "Detection of gas bubble leakage via correlation of water column multibeam images," *Ocean Sci.*, vol. 8, no. 2, pp. 175–181, 2012.
[22] T. Weber *et al.*, "Mapping gas seeps with the deepwater multibeam echosounder on Okeanos Explorer," *Oceanography*, vol. 25, no. S1, pp. 657–661, 2012.
[23] A. Skarke, C. Ruppel, M. Kodis, D. Brothers, and E. Lobecker, "Widespread methane leakage from the sea floor on the northern US Atlantic margin," *Nature Geosci.*, vol. 7, no. 9, pp. 657–661, 2014.
[24] P. Urban, K. Köser, and J. Greinert, "Processing of multibeam water column image data for automated bubble/seep detection and repeated mapping," *Limnol. Oceanogr., Methods*, vol. 15, no. 1, pp. 1–21, 2017.
[25] C. S. Clay and H. Medwin, *Acoustical Oceanography: Principles and Applications*. New York, NY, USA: Wiley, 1977.
[26] A. Schimel, C. Brown, and D. Ierodiaconou, "Automated filtering of multibeam water-column data to detect relative abundance of giant kelp (Macrocystis pyrifera)," *Remote Sens.*, vol. 12, no. 9, pp. 1–20, 2020.
[27] C. de Moustier, "OS-CFAR detection of targets in the water column and on the seafloor with a multibeam echosounder," in *Proc. OCEANS Conf.*, San Diego, CA, USA, 2013, pp. 1–2.
[28] C. de Moustier, "Detection and clustering of acoustic backscatter from hydrothermal vent plumes, in *Proc. MTS/IEEE OCEANS Conf.*, Seattle, WA, USA, 2019, pp. 1–5.
[29] M. A. Richards, *Fundamentals of Radar Signal Processing*. New York, NY, USA: McGraw-Hill, 2005, pp. 347–383.
[30] D. A. Abraham, *Underwater Acoustic Signal Processing: Modeling, Detection, and Estimation*. Berlin, Germany: Springer, 2019, pp. 562–584.
[31] H. Rohling, "Radar CFAR thresholding in clutter and multiple target situations," *IEEE Trans. Aerosp. Electron. Syst.*, vol. AES-19, no. 4, pp. 608–621, Jul. 1983.
[32] P. P. Gandhi and S. A. Kassam, "Analysis of CFAR processors in non-homogeneous background," *IEEE Trans. Aerosp. Electron. Syst.*, vol. 24, no. 4, pp. 427–445, Jul. 1988.
[33] B. Y. Mills and A. G. Little, "A high-resolution aerial system of a new type," *Aust. J. Phys.*, vol. 6, no. 3, pp. 272–278, 1953.
[34] X. Lurton, *An Introduction to Underwater Acoustics: Principles and Applications*, 2nd ed. Berlin, Germany: Springer, 2010, pp. 351–369.
[35] T. L. Hopkins, "The composition and standing stock of mesopelagic micronekton at 27°N 86°W in the eastern Gulf of Mexico," *Contrib. Mar. Sci.*, vol. 27, pp. 143–158, 1984.
[36] J. S. Bendat and A. G. Piersol, *Random Data: Analysis and Measurement Procedures*. Hoboken, NJ, USA: Wiley, 2000, pp. 105–108.
[37] D. A. Abraham and A. P. Lyons, "Simulation of non-Rayleigh reverberation and clutter," *IEEE J. Ocean. Eng.*, vol. 29, no. 2, pp. 347–362, Apr. 2004.
[38] J. R. Preston and D. A. Abraham, "Non-Rayleigh reverberation characteristics near 400 Hz observed on the New Jersey shelf," *IEEE J. Ocean. Eng.*, vol. 29, no. 2, pp. 215–235, Apr. 2004.
[39] R. Clift, J. R. Grace, and M. E. Weber, *Bubbles, Drops, and Particles*. New York, NY, USA: Academic, 1978, pp. 169–199.

Thomas C. Weber (Member, IEEE) received the B.S. and M.S. degrees in ocean engineering from the University of Rhode Island, Kingston, RI, USA, in 1997 and 2000, respectively, and the Ph.D. degree in acoustics from the Pennsylvania State University, State College, PA, USA, in 2006.

He was a Research Assistant Professor in Ocean Engineering from 2006 to 2012, and an Assistant Professor of Mechanical Engineering from 2012 to 2017, all at the University of New Hampshire, Durham, NH, USA, where he is currently an Associate Professor of Mechanical and Ocean Engineering. He is a member of the UNH Center for Coastal and Ocean Mapping and the UNH Center for Ocean Engineering.

Dr. Weber is a member of the Acoustical Society of America and the IEEE Oceanic Engineering Society.